Chemical Science

ROYAL SOCIETY OF CHEMISTRY

EDGE ARTICLE

View Article Online
View Journal

Check for updates

Cite this: DOI: 10.1039/d6sc02317g

All publication charges for this article have been paid for by the Royal Society of Chemistry

Open Access Article. Published on 15 April 2026. Downloaded on 5/6/2026 4:13:05 AM. This article is licensed under a Creative Commons Attribution-NonCommercial 3.0 Unported Licence.

Programmable wavelength- and time-dependent multicolor afterglow in polyvinyl alcohol *via* synergistic ion-bridging and crosslinking interactions

Shukang Yang,[a] Ying Lv,[a] Guorui Zhai,[a] Xiaohui Yu,[b] Jinmei Du,[a] Yang Jiang,[a] Dagang Miao,[a] Guowei Xiao *[a] and Changhai Xu *[a]

Time-dependent multicolor afterglow (TDMA) introduces a temporal dimension to optical encoding, enabling dynamically distinguishable visual outputs beyond the capability of static emission or single-color persistent luminescence. Nevertheless, the rational construction of TDMA systems remains highly challenging because it requires the simultaneous generation and precise regulation of multiple long-lived emissive states within one material. Herein, we propose a strategy of introducing ion-bridging interactions into a covalently crosslinked monochromatic persistent luminescence system. The ion-induced interactions partially reorganize the original covalent/hydrogen-bonding network and generate new rigid microenvironments; these Na^+-associated microdomains, together with the pre-existing crosslinked domains, cooperatively generate emissive centers to form dynamic phosphorescent polymers. As a result, the initially static single-color afterglow evolves into wavelength- and time-dependent dynamic multicolor afterglow maintaining an ultralong RTP lifetime of 1.06 s. Notably, by tuning the excitation wavelengths within a narrow 15 nm window (385–400 nm), the afterglow can be modulated over more than 100 nm (460–563 nm), affording a distinct color evolution from yellow-green to cyan to blue. This work provides a practical framework for achieving wavelength/time regulation of dynamic multicolor afterglow in host–guest systems and offers a visual platform for accurate energy discrimination, with promising potential in multilevel information encryption and optoelectronic applications.

Received 20th March 2026
Accepted 14th April 2026

DOI: 10.1039/d6sc02317g

rsc.li/chemical-science

Introduction

The rapid advancement of information technology has led to an exponential surge in the volume of information, making it increasingly challenging to discern its authenticity and accuracy.[1–3] As the cornerstone for driving the iterative upgrading of information encryption technologies, advanced intelligent information encryption materials urgently require further development. In the realm of photo-functional materials, the relentless pursuit of advanced information security and photonic technologies has driven the evolution of luminescent materials from static emitters to dynamic, multi-dimensional systems.[4,5] Particularly, luminescent materials represented by organic room-temperature phosphorescence (RTP) materials have become a research hotspot in the field of optoelectronic materials owing to their notable advantages such as high design flexibility in molecular structure, excellent mechanical flexibility, and outstanding biocompatibility.[6,7] Among these, materials exhibiting TDMA have emerged as a particularly compelling class.[8,9] These materials display visually distinguishable color evolution after removal of the excitation source, and can introduce a temporal dimension into the optical readout and thus significantly enhance the level of information encryption, anti-counterfeiting, and dynamic display.[10–12]

Current TDMA strategies generally rely on constructing multiple phosphorescent centers with distinct emission energies and decay kinetics in a single system.[13,14] Early examples were mainly based on the physical mixture of inorganic phosphors containing rare earth ions, and although effective in producing multicolor afterglow, such systems often suffer from phase separation, uncontrolled energy transfer, and poor processability.[15–17] Organic RTP systems have emerged as promising alternatives owing to their structural tunability and molecular-level designability.[18] At the single-molecule level, conformational engineering has enabled intrinsic dual long-lived emission and time-dependent color evolution. For instance, Zhu *et al.* realized red-to-green afterglow conversion

[a]College of Textiles & Clothing, Qingdao University, Qingdao, Shandong 266071, P. R. China. E-mail: gwxiao@qdu.edu.cn; changhai_xu@qdu.edu.cn
[b]Jiangsu Lianfa Textile Co, Ltd, Nantong, Jiangsu 226400, P. R. China

© 2026 The Author(s). Published by the Royal Society of Chemistry

Open Access Article. Published on 15 April 2026. Downloaded on 5/6/2026 4:13:05 AM. This article is licensed under a Creative Commons Attribution-NonCommercial 3.0 Unported Licence.

by integrating flexible C–S–C rotors into a rigid aromatic framework, where different conformers generated emissive states with distinct lifetimes.[19,20] Chi *et al.* achieved TDMA by coupling thermally activated delayed fluorescence (TADF) and RTP within one molecular system.[11] However, in such a system, a tightly bound singlet-triplet energy gap (ΔE_{ST}) is needed to couple TADF from the excited single state (S_1) with RTP from the excited triplet state (T_1), leaving limited freedom for spectral or kinetic modulation.[21,22] Beyond single-component systems, crystal engineering,[23] polymerization,[24–26] host–guest doping and matrix engineering[27] have also been reported to construct TDMA materials. In particular, the rational design and precise modulation of organic host–guest systems offer significant potential for realizing TDMA properties.[6,24,28]

As a common water-soluble polymer, poly(vinyl alcohol) (PVA) contains a large number of hydroxyl groups (–OH) in its molecular chain, which can form stable composite systems with guest luminescent molecules through hydrogen bonding or covalent bonding. In addition, PVA-based films possess good flexibility and transparency, facilitating subsequent processing and application, and have been widely used to construct flexible RTP materials.[29–31] Among the color regulation strategies of organic RTP materials, metal ion regulation has attracted much attention due to its simplicity and significant regulation effect.[32,33] Existing studies mainly focus on transition metal ions (such as Cd^{2+} and Zn^{2+}) changing the electronic configuration and excited-state energy levels of guest molecules through coordination, thereby realizing color regulation.[26,32] In contrast, alkali metal ions (such as Na^+ and K^+) have not been fully developed in RTP regulation due to their small ionic radius, moderate charge density, wide availability, and low cost. Previous studies have shown that alkali metal ions can affect the stacking state and excited-state dynamics of guest molecules through ion–dipole interactions,[34–36] but their application in RTP modulation of polymer materials, especially by regulating the triplet energy levels to achieve color control, is still scarce. In addition, the color regulation of most polymer-based RTP materials relies on complex molecular design or harsh preparation conditions, which makes it difficult to meet the requirements of large-scale applications.[37–39] Therefore, developing color-tunable RTP materials based on simple blending and low-cost regulators is of great practical significance.[40–42]

Herein, we adopt a salt-induced network-reorganization strategy to realize wavelength- and time-dependent multicolor afterglow in a PVA-based host–guest system. We soaked the PVA polymer solutions in the NaCl solutions. Cl^- can polarize the hydration water molecules *via* the Hofmeister effect, which breaks hydrogen bond between the hydroxyl groups, and hydroxyl oxygen further binds to 4-(bis(4-methoxyphenyl) amino)phenylboronic acid (4-omPA) through Na^+-bridging interactions, breaking the original covalent crosslinking system PVA/4-omPA and constructing new multiple triplet states, thereby obtaining a multi-channel dynamic color adjustable afterglow from yellow green to blue and cyan to blue under different excitations, and finally to blue within the polymer matrix (Fig. 1 and S1). In contrast, PVA/4-omPA with only covalent crosslinking and hydrogen bonding does not possess such tunability. This study provides a new idea for the development of multifunctional and low-cost flexible RTP materials, and the prepared color-tunable RTP films have potential applications in flexible displays, information anti-counterfeiting, and other fields.

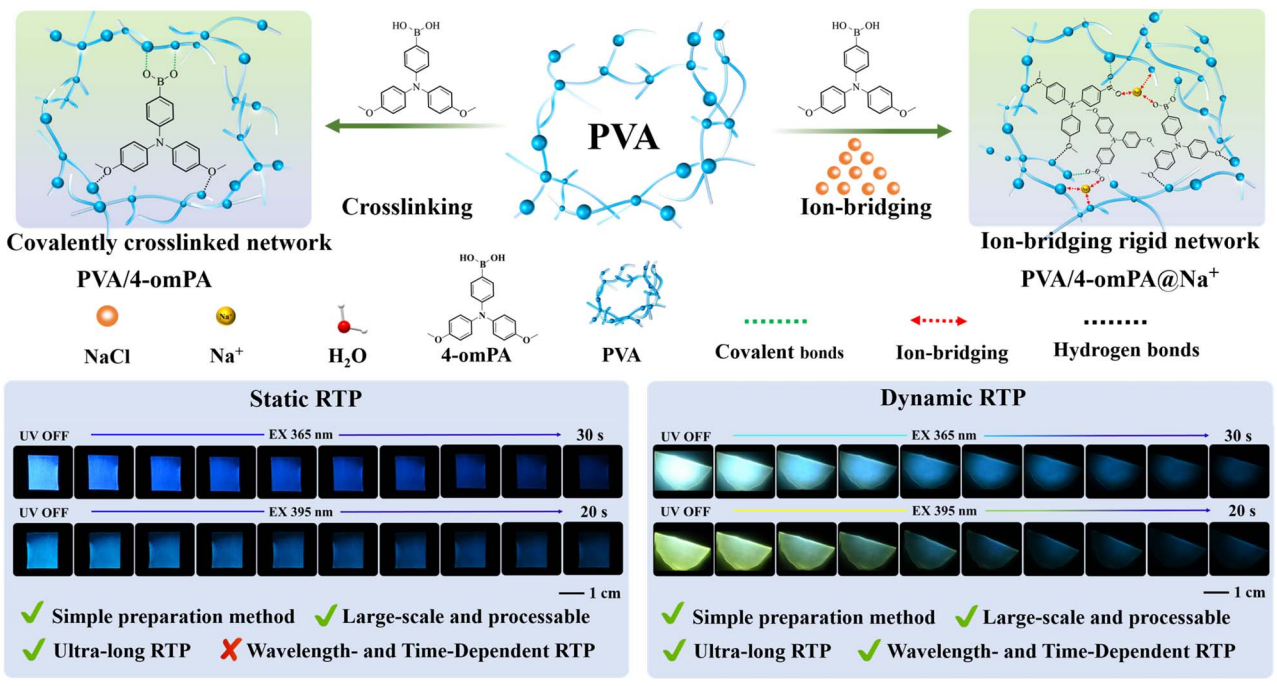

Fig. 1 Schematic representation of the synthesis of PVA/4-omPA and PVA/4-omPA@Na^+, and their corresponding afterglow images after turning off the 365 nm and 395 nm UV lamp.

© 2026 The Author(s). Published by the Royal Society of Chemistry

Open Access Article. Published on 15 April 2026. Downloaded on 5/6/2026 4:13:05 AM.
This article is licensed under a Creative Commons Attribution-NonCommercial 3.0 Unported Licence.

Results and discussion

Photophysical properties

The photophysical properties of 4-omPA, and the optimized PVA/4-omPA and PVA/4-omPA@Na^+ films were studied *via* photoluminescence (PL) spectroscopy in both prompt and delayed (acquired after 1 ms of excitation) modes. For 4-omPA, under 365 nm excitation, the powder exhibits blue fluorescence (FL) at 450 nm. After removing the excitation, the phosphorescence intensity of 4-omPA is weak and no phosphorescence emission is observed (Fig. S2). For PVA/4-omPA, the film shows blue FL at 450 nm under 365 nm excitation (Fig. S3a), and after removing the excitation, the PVA/4-omPA film shows only a long-lived blue afterglow. The delayed PL mapping spectra indicate that the phosphorescence emission peaks consistently appear within the 460–465 nm range on increasing the excitation wavelengths from 280 nm to 395 nm (Fig. 2a). This behavior is consistent with the corresponding Commission Internationale de l'Eclairage (CIE) coordinates, which remain in the blue region irrespective of the excitation wavelength, indicating that PVA/4-omPA behaves as a monochromatic RTP system (Fig. 2b and Table S2). The observed behavior originates from the cooperative covalent crosslinking and hydrogen bonding between PVA and 4-omPA, which rigidifies the matrix and suppresses molecular motion, thereby stabilizing a single triplet emissive state in PVA/4-omPA. Meanwhile, the N/O/B-containing framework favors n–π* orbital mixing and promotes intersystem crossing, enabling efficient population of long-lived triplet states with a lifetime of up to 1.38 s (Fig. 2c and Table S1). For PVA/4-omPA@Na^+, the fluorescence of the film shows blue emission (Fig. S3b). In contrast to the single phosphorescence emission peak observed in PVA/4-omPA, the delayed PL spectra of PVA/4-omPA@Na^+ exhibit new emission peaks at 460 nm, 530 nm and 563 nm (Fig. 2d). After removing the 365 nm and 395 nm UV lamp, cyan and yellow phosphorescence emissions were observed, respectively, exhibiting excitation wavelength-dependent afterglow (Fig. 2e and Table S3). The decay curves of PVA/4-omPA@Na^+ for the two emissions exhibit 1.06 s and 0.794 s at 460 nm and 530 nm, respectively (Fig. 2f).

To deeply investigate the dependence of dual emission peaks on the excitation wavelength, phosphorescence spectra were recorded across excitation wavelengths ranging from 280 to 400 nm. At excitation wavelengths between 280 and 385 nm, the emission peak at 460 nm exhibited strong intensity, whereas the emission peaks at 530 nm and 563 nm were comparatively weak (Fig. S4). As the excitation wavelengths are increased to 390–395 nm, however, the relative intensities are reversed and the 530 nm emission becomes predominant, while the 460 nm band is markedly attenuated (Fig. 2d). The PVA/4-omPA@Na^+ films can be excited in a narrow wavelength range from 385 nm to 395 nm, which shows their sensitivity to energy. More interestingly, the PVA/4-omPA@Na^+ film not only exhibits excitation wavelength-dependent afterglow but also shows dynamic color evolution over time. After the UV lamp is removed, the afterglow evolves from bright cyan to blue under 365 nm excitation and from yellow-green to cyan to blue under 395 nm excitation, with the dynamic process remaining visible for up to 30 s under ambient conditions (Fig. 1).

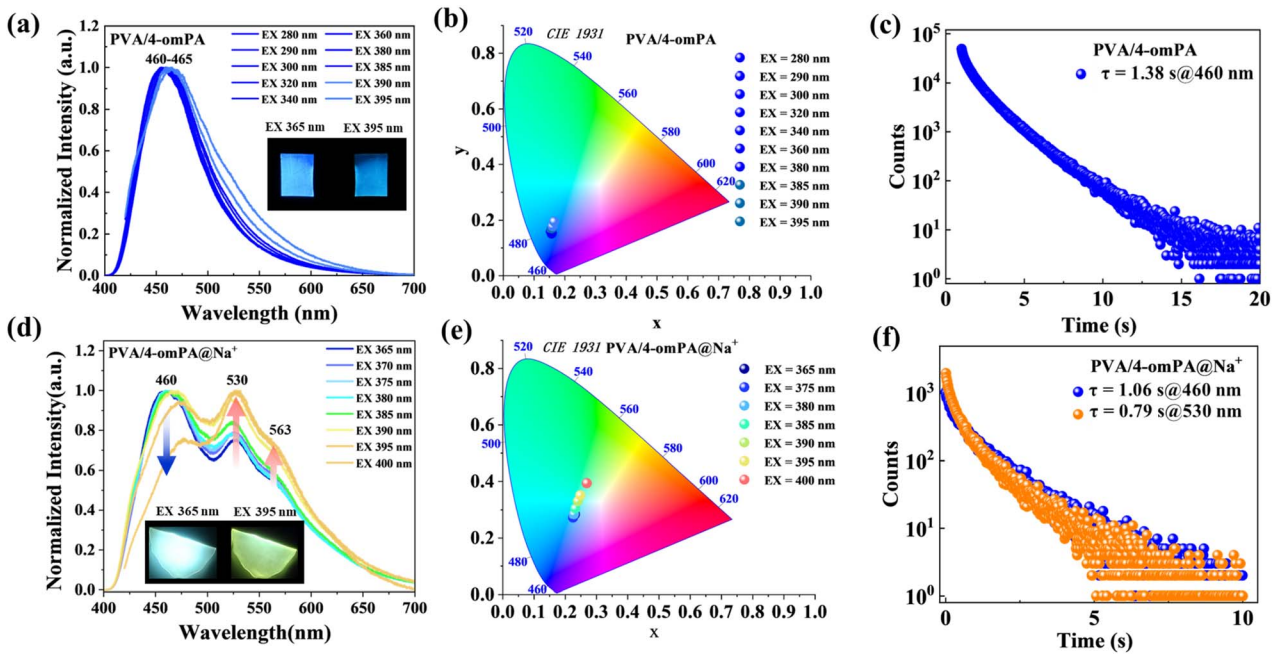

Fig. 2 Photophysical properties of 4-omPA-doped materials under ambient conditions. (a) Excitation-phosphorescence mapping of PVA/4-omPA under ambient conditions. (b) CIE coordinate diagram of PVA/4-omPA by changing the excitation wavelengths. (c) Time-resolved decay profiles at 460 nm. (d) Excitation-phosphorescence mapping of PVA/4-omPA@Na^+ under ambient conditions. (e) CIE coordinate diagram of PVA/4-omPA@Na^+ on changing the excitation wavelengths. (f) Time-resolved decay profiles at 460 nm and 530 nm.

Open Access Article. Published on 15 April 2026. Downloaded on 5/6/2026 4:13:05 AM.
This article is licensed under a Creative Commons Attribution-NonCommercial 3.0 Unported Licence.

TDMA of the PVA/4-omPA@Na^+ film

To investigate the dynamic evolution characteristics of afterglow in PVA/4-omPA@Na^+, the time-resolved delay spectra confirm the TDMA evolution from cyan to blue and yellow-green to blue in the PVA/4-omPA@Na^+ films under 365 nm and 395 nm excitation, respectively (Fig. 3). Under 395 nm excitation, at a delay time of 0.5 s, the main emission peaks are observed at 460 and 530 nm, displaying a yellow-green phosphorescent color due to the combination of yellow and blue light. As the delay time continued to increase, the relative intensity at 460 nm further increased, and the phosphorescent color shifted toward blue. At a delay time of 2 s, a cyan mixed phosphorescent color was observed due to the comparable intensity of yellow and blue light. When the decay time reaches 5 s, only a blue 460 nm phosphorescence peak is displayed, exhibiting a blue phosphorescence color (Fig. 3a and c). The phosphorescence lifetime at 530 nm (green emission) is relatively shorter (0.79 s), whereas the lifetime at 460 nm (blue emission) is longer (1.06 s) (Fig. 2f). Thus, yellow-green phosphorescence emission initially dominates but quickly decays. Over time, the intensity of the blue phosphorescence surpasses that of the yellow emission leading to a significant yellow-green to blue TDMA. This results in a wavelength shift of up to 70 nm, consistent with the color change path in the corresponding CIE chromaticity diagram (Fig. 3b and Table S4). Under 365 nm excitation, the phenomenon of TDMA was also observed in the PVA/4-omPA@Na^+ films, and its time-resolved delay spectra showed a significant color change in the afterglow color from cyan to blue as the delay time increased from 0.5 s to 5 s (Fig. 3d–f and Table S5).

Importantly, the introduction of NaCl did not reconstruct the main chromophore itself, but further reshaped the local electronic environment and network rigidity through ion-bridging interactions between Na^+ and oxygen-rich sites. This reorganization generates the formation of multiple distinct microenvironments, subsequently generating different triplet energy levels. Different excitation wavelengths can preferentially excite energy matched excited states, and based on the decay rates of different lifetimes, PVA/4-omPA@Na^+ exhibits significant excitation wavelength-dependent multicolor phosphorescence and dynamic afterglow evolution on a time scale. To evaluate the generality of this strategy, Na^+ was replaced by K^+ and Mg^{2+}, and both PVA/4-omPA@K^+ and PVA/4-omPA@Mg^{2+} likewise exhibit wavelength- and time-dependent multicolor afterglow, supporting the broader applicability of this ion-regulated approach (Fig. S5 and S6).

Structural characterization

To elucidate the origin of the afterglow emission, the samples were systematically investigated using multiple characterization

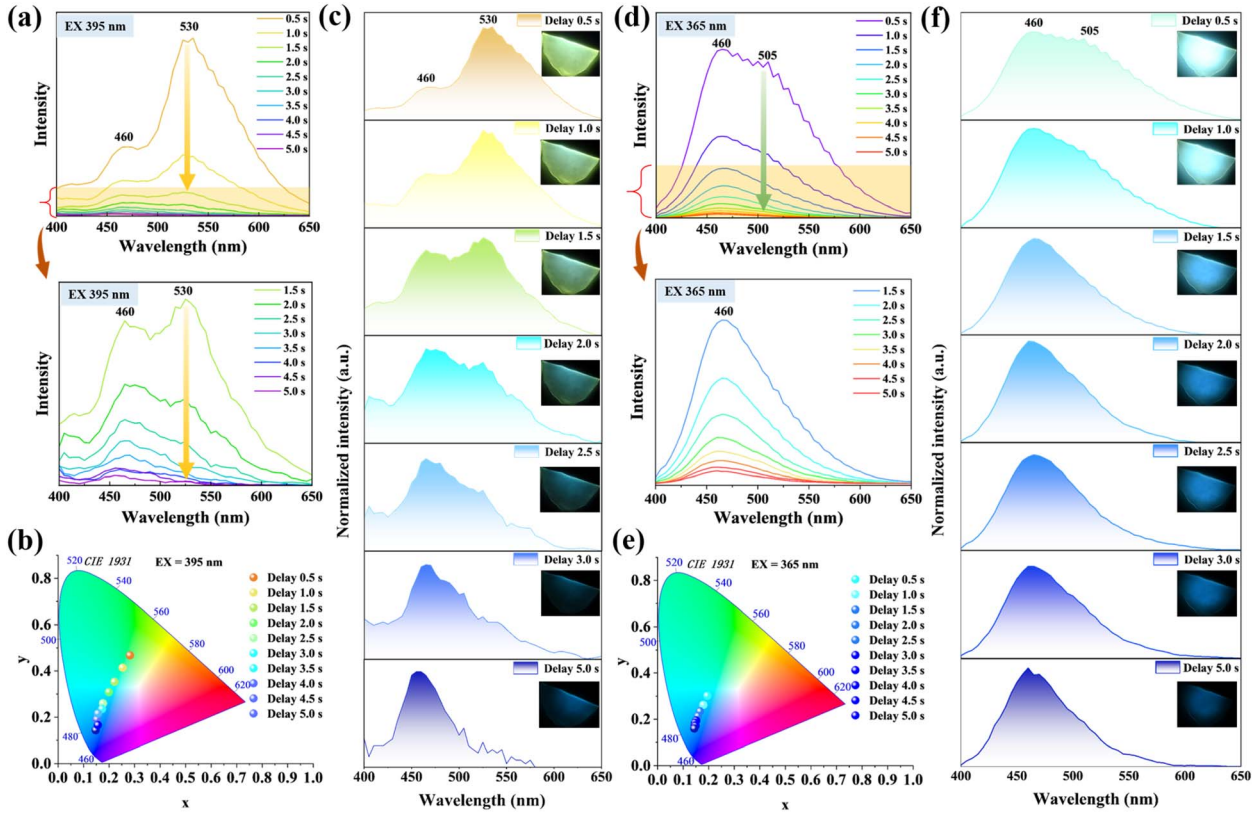

Fig. 3 (a and d) Unnormalized time-resolved emission spectra recorded after switching off the 395 nm and 365 nm UV lamp, with delay times from 0.5 to 5.0 s. (b and e) Corresponding CIE chromaticity coordinates derived from the spectra (a) and (d), illustrating the time-dependent color evolution. (c and f) Normalized time-resolved emission spectra at selected delay times (0.5–5.0 s) under 365 nm and 395 nm excitation, revealing the gradual spectral shift during the decay process, with inset photographs showing the afterglow emission at different delay times.

© 2026 The Author(s). Published by the Royal Society of Chemistry

Open Access Article. Published on 15 April 2026. Downloaded on 5/6/2026 4:13:05 AM.
This article is licensed under a Creative Commons Attribution-NonCommercial 3.0 Unported Licence.

techniques. As shown in Fig. 4a, the UV-vis spectrum of pristine PVA shows absorption features centered at 224 and 285 nm, which are typical of defect-related transitions in PVA, assigned to n → π* transitions. In contrast, 4-omPA exhibits a 390 nm dominant long-wavelength absorption. Given its triphenylamine-derived electron-donating core and aryl boronic acid substituent, this band is assigned to a charge-transfer-dominated (π–π*) transition with significant intramolecular charge-transfer (ICT) character. After reaction with PVA, the maximum absorption of the film shifts from 390 nm for 4-omPA to 355 nm for PVA/4-omPA. This substantial blue shift strongly suggests that 4-omPA is not merely physically dispersed in PVA, but instead experiences a distinct electronic reorganization upon incorporation into the polymer matrix. It is the formation of boronate ester linkages between the boronic acid moiety and PVA diols, which changes the boron-centered electronic environment, attenuates the original donor–acceptor ICT character, and simultaneously constrains chromophore relaxation within the network. For PVA/4-omPA@Na^+, the absorption maximum moves only slightly from 355 to 359 nm. This much smaller shift indicates that Na^+ does not generate a new chromophoric skeleton, but instead tunes the local environment of the pre-existing emissive network by ion-bridging interactions.

Subsequently, the intermolecular interactions within the three films were investigated by using Fourier transform infrared (FT-IR) spectra (Fig. 4b). Pristine PVA shows a broad and intense band centered at 3260 cm^{-1}, which is assigned to O–H stretching of the hydroxyl-rich polymer networks,[43] together with a characteristic band at 1144 cm^{-1} corresponding to C–O stretching in the PVA backbone.[44,45] Upon covalent cross-linking with 4-omPA, the intensity of the O–H stretching band at 3260 cm^{-1} is significantly diminished. This reduction confirms the consumption of hydroxyl groups through the formation of boronate ester bonds (B–O–C) between PVA and the boronic acid moieties of 4-omPA.[46] The intensity of the C–O stretching vibration peak at 1144 cm^{-1} in the PVA main chain decreases, indicating that the cross-linking effect has disrupted some crystalline regions of the PVA main chain. At the same time, a new peak at 1327 cm^{-1} is observed, which is attributed to the asymmetric stretching vibration of the B–O–C bond in the borate ester, indicating that 4-omPA has successfully covalently cross-linked with PVA. Following the introduction of NaCl to form PVA/4-omPA@Na^+, the further attenuation of the O–H band at 3260 cm^{-1} suggests that Na^+-bridging interactions also influence the hydrogen bonding network of the remaining hydroxyl groups.[47] The B–O stretching peak at 1327 cm^{-1} shifts to a lower wavenumber of 1270 cm^{-1}. This red-shift is attributed to the ion-bridging interactions of Na^+ with the boron atoms, which alters the electron density of the B–O bonds within the boronate ester groups.

Powder X-ray diffraction (XRD) was employed to characterize the structural evolution of PVA, PVA/4-omPA, and PVA/4-omPA@Na^+ (Fig. 4c). PVA displays a characteristic broad diffraction peak at 19.5°, corresponding to its semicrystalline hydrogen-bonded packing. After incorporation of 4-omPA, additional shoulder features emerge at approximately 23°, indicating that the PVA packing is reorganized and new short-range ordered domains are generated upon boronate-ester-

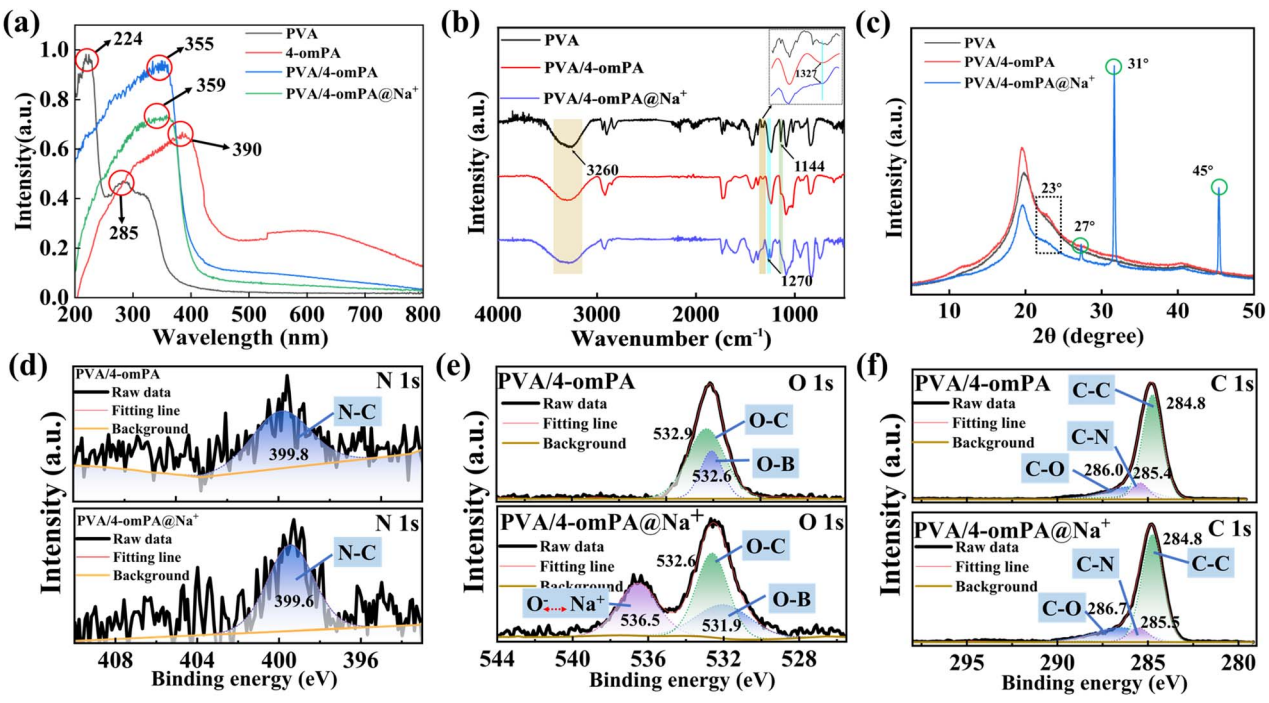

Fig. 4 Structural characterization of the composite films. (a) UV-vis absorption curves of PVA, 4-omPA, PVA/4-omPA, and PVA/4-omPA@Na^+. (b) FT-IR spectra and (c) XRD patterns of PVA, PVA/4-omPA and PVA/4-omPA@Na^+. (d–f) High-resolution XPS spectra of N 1s, O 1s, and C 1s for PVA/4-omPA and PVA/4-omPA@Na^+.

Open Access Article. Published on 15 April 2026. Downloaded on 5/6/2026 4:13:05 AM. This article is licensed under a Creative Commons Attribution-NonCommercial 3.0 Unported Licence.

mediated crosslinking. Upon NaCl treatment, sharp reflections appear at around 31° and 45°, matching well with the characteristic diffraction peaks of crystalline NaCl. Therefore, NaCl not only adjusts the crosslinked polymer network but also exists partly in the crystalline form. DSC-TGA further demonstrates that both PVA/4-omPA and PVA/4-omPA@Na^+ decompose more gradually than pristine PVA, as evidenced by their reduced mass-loss rates during thermal degradation (Fig. S7). This behavior indicates that in the PVA/4-omPA film, covalent crosslinking between 4-omPA and the PVA matrix contributes to enhanced structural rigidity. Furthermore, in the PVA/4-omPA@Na^+ system, the Na^+-induced ion-bridging interactions, together with the intrinsic covalent crosslinking between 4-omPA and PVA, synergistically reinforce the internal rigid environment of the polymer network, thereby improving the overall thermal stability of the material. From the energy dispersive X-ray spectroscopy (EDS) of PVA/4-omPA and PVA/4-omPA@Na^+, it can be seen that the elements C, O, N, B, Na, and Cl are evenly distributed in the composite material (Fig. S8 and S9). This indicates that the guest molecules and NaCl do not aggregate in the material, and thus will not cause errors in the spectral collection.

High-resolution XPS spectra of N 1s, O 1s, and C 1s were collected to elucidate the chemical-state evolution from PVA/4-omPA to PVA/4-omPA@Na^+ (Fig. S10 and S11). The N 1s spectra of both samples exhibit a dominant peak at 399.6–399.8 eV, characteristic of aryl amine (C–N) in the triphenylamine unit, confirming successful incorporation of 4-omPA into the polymer matrix. Notably, the N 1s line shape remains nearly unchanged after NaCl treatment, indicating that Na^+ does not significantly interact with the nitrogen center (Fig. 4d). In the O 1s region of PVA/4-omPA, two components are observed: a peak

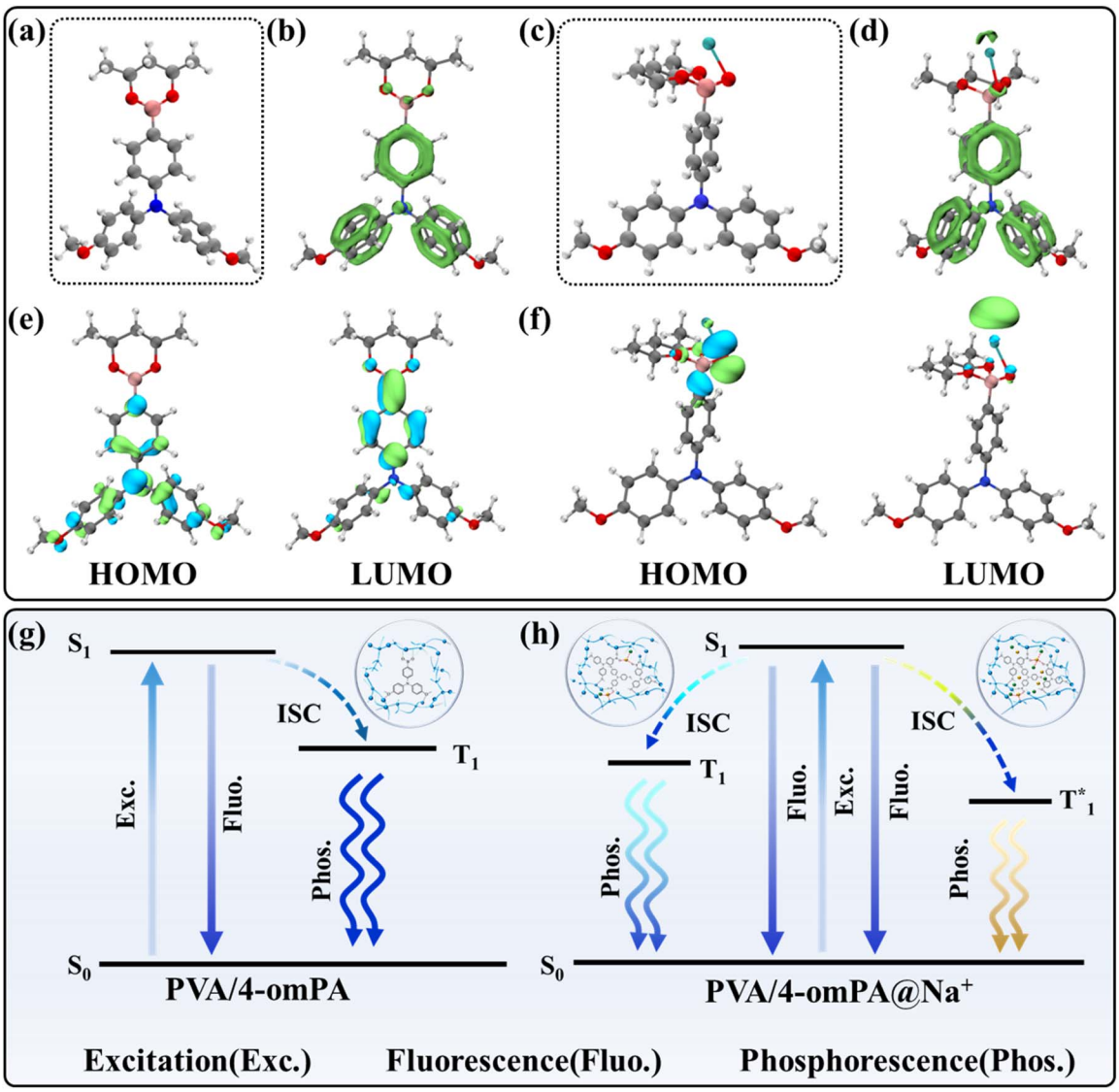

Fig. 5 (a and c) Idealized structural models of the PVA/4-omPA and PVA/4-omPA@Na^+ systems used for theoretical calculations. (b and d) Locator-π (LOL-π) isosurfaces. (e and f) Frontier molecular orbital distributions (HOMO and LUMO) of PVA/4-omPA and PVA/4-omPA@Na^+. (g and h) Schematic diagrams of the photophysical mechanisms for PVA/4-omPA and PVA/4-omPA@Na^+ systems.

© 2026 The Author(s). Published by the Royal Society of Chemistry

Open Access Article. Published on 15 April 2026. Downloaded on 5/6/2026 4:13:05 AM. This article is licensed under a Creative Commons Attribution-NonCommercial 3.0 Unported Licence.

at 532.6–532.9 eV assigned to C–O species (alcohol/ether oxygen from the PVA backbone) and a lower-binding-energy peak at ~531.9–532.6 eV attributed to boron-associated oxygen, consistent with the formation of boronate-type crosslinking between PVA diols and boronic acid groups. After NaCl treatment, the binding energies of C–O (532.6 eV) and B–O (531.9 eV) in the PVA/4-omPA@Na^+ films have shifted towards lower energy compared to those of PVA/4-omPA, indicating the formation of a new oxygen related low binding energy environment.[48] An additional high-binding-energy feature appears at 536.5 eV, indicating a modified oxygen environment associated with Na^+ incorporation (Fig. 4e). The C 1s spectra can be deconvoluted into peaks at 284.8 eV (C–C/C=C), 285.4 eV, 285.5 eV (C–N), and 286.0 eV, 286.7 eV (C–O). Importantly, the overall C 1s profile remains largely unchanged after NaCl treatment, indicating that Na^+ mainly modulates the oxygen-rich crosslinked network without reconstructing the organic carbon framework (Fig. 4f). Together, the XPS results support a boronate-type covalently crosslinked PVA/4-omPA network, while the spectral evolution in O 1s after NaCl treatment indicates formation of a Na^+-bridged microenvironment within the polymer matrix.[49]

Overall, these structural characterization studies show that incorporation of 4-omPA reconstructs the local PVA microenvironment through boronate-type covalent crosslinking and an extended hydrogen-bonding network, thereby enabling long-lived blue phosphorescence from PVA/4-omPA. Subsequent NaCl treatment further reorganizes this oxygen-rich framework through Na^+-bridging interactions without altering the fundamental chromophoric skeleton. The resulting hierarchical network simultaneously rigidifies the guest emitter and diversifies the local electronic environment, thereby generating multiple triplet microstates with different energies and decay kinetics. This cooperative structural reorganization provides a reliable basis for the excitation wavelength/time-dependent afterglow observed in PVA/4-omPA@Na^+.

Theoretical calculation

To gain insight into the interaction between Na^+ and the host–guest system, an idealized model was constructed containing the 4-omPA guest molecule together with a representative PVA fragment covalently connected to the guest (Fig. 5a). The electrostatic potential (ESP) map reveals that the B–O bond region and the methoxy oxygen (O–Me) exhibit pronounced blue regions, indicating high electron density (Fig. S12). These electron-rich sites therefore represent potential adsorption sites for Na^+ ions. However, in the polymer matrix, the methoxy oxygen atoms preferentially form hydrogen-bonding interactions with the surrounding PVA network, which decreases their tendency to bridge with Na^+. Consequently, the B–O region becomes a more favorable binding site for Na^+. Considering that Na^+ is a typical hard Lewis acid and preferentially coordinates with hard bases such as oxygen atoms rather than the electron-deficient boron center, Na^+ is likely to interact with the boron moiety through an oxygen bridge, forming a Na^+-mediated O–B bridging structure (Fig. 5c). The bridging effect of Na^+ also induces a significant structural transformation of the boron center. The boron atom has a typical sp^2 hybridization structure, allowing the B–O unit to partially participate in electron conjugation without Na^+. After the boron center is bridged by Na^+, it transforms into an sp^3 hybridization structure, resulting in the formation of a tetrahedral structure. This conformational change disrupts the original conjugation pathway and alters the electronic distribution of the system, thereby affecting the photophysical properties of the guest molecule.

To further elucidate the influence of Na^+-bridging interactions on the electronic structure, the localized orbital locator-π (LOL-π) analysis was performed to visualize the changes in π-electron delocalization. For PVA/4-omPA, noticeable π-electron density remains distributed around the B–O region, indicating that this unit partially participates in the conjugated electronic system (Fig. 5b). After the introduction of Na^+, the Na^+-bridging interactions induce a pronounced geometric distortion at the boron center, transforming the originally planar sp^2 configuration into a tetrahedral sp^3 structure. This structural change significantly suppresses the π-electron delocalization around the B–O unit and weakens the conjugation pathway by hindering effective orbital overlap (Fig. 5d).

Frontier molecular orbital analysis further reveals that Na^+-bridging interactions substantially alter the electronic structure. In the Na^+-free system, both the HOMO and LUMO are mainly localized on the *N*-$(phenyl)_3$ fragment, whereas after Na^+-bridging the frontier orbitals redistribute toward the B–O and B–O–Na regions (Fig. 5e and f), accompanied by a significant reduction of the HOMO–LUMO gap from 4.17 to 2.74 eV (Fig. S13). This electronic redistribution generates additional triplet emissive centers associated with the B–O–Na unit, while the intrinsic triplet state of the aromatic framework remains preserved. The coexistence of these emissive states with different energies and decay pathways creates multiple phosphorescence channels, ultimately leading to the wavelength- and time-dependent multicolor afterglow observed in the PVA/4-omPA@Na^+ system (Fig. 5g and h).

Time-resolved coding for data storage encryption

Owing to the excellent processability, high transparency and multidimensional optical properties of intelligent phosphorescent polymer composites, we have explored their applications in information encryption and anti-counterfeiting (Fig. S14). Fig. 6 demonstrates the utilization of PVA, PVA/4-omPA, and PVA/4-omPA@Na^+ materials in logic-gate-based information encryption and storage. Leveraging ASCII coding alongside the distinct photophysical characteristics of these three phosphorescent materials under 395 nm excitation, an encryption algorithm was developed, as depicted in Fig. 6a. After removing the 395 nm excitation, the algorithm initially outputs the first set of ASCII data based on the criterion of "presence or absence of phosphorescence emission", generating the binary sequences "01010001", "01000100", and "01010101", which correspond to the combined message "QDU". Notably, due to the time-dependent afterglow behavior of the PVA/4-omPA@Na^+

Open Access Article. Published on 15 April 2026. Downloaded on 5/6/2026 4:13:05 AM.
This article is licensed under a Creative Commons Attribution-NonCommercial 3.0 Unported Licence.

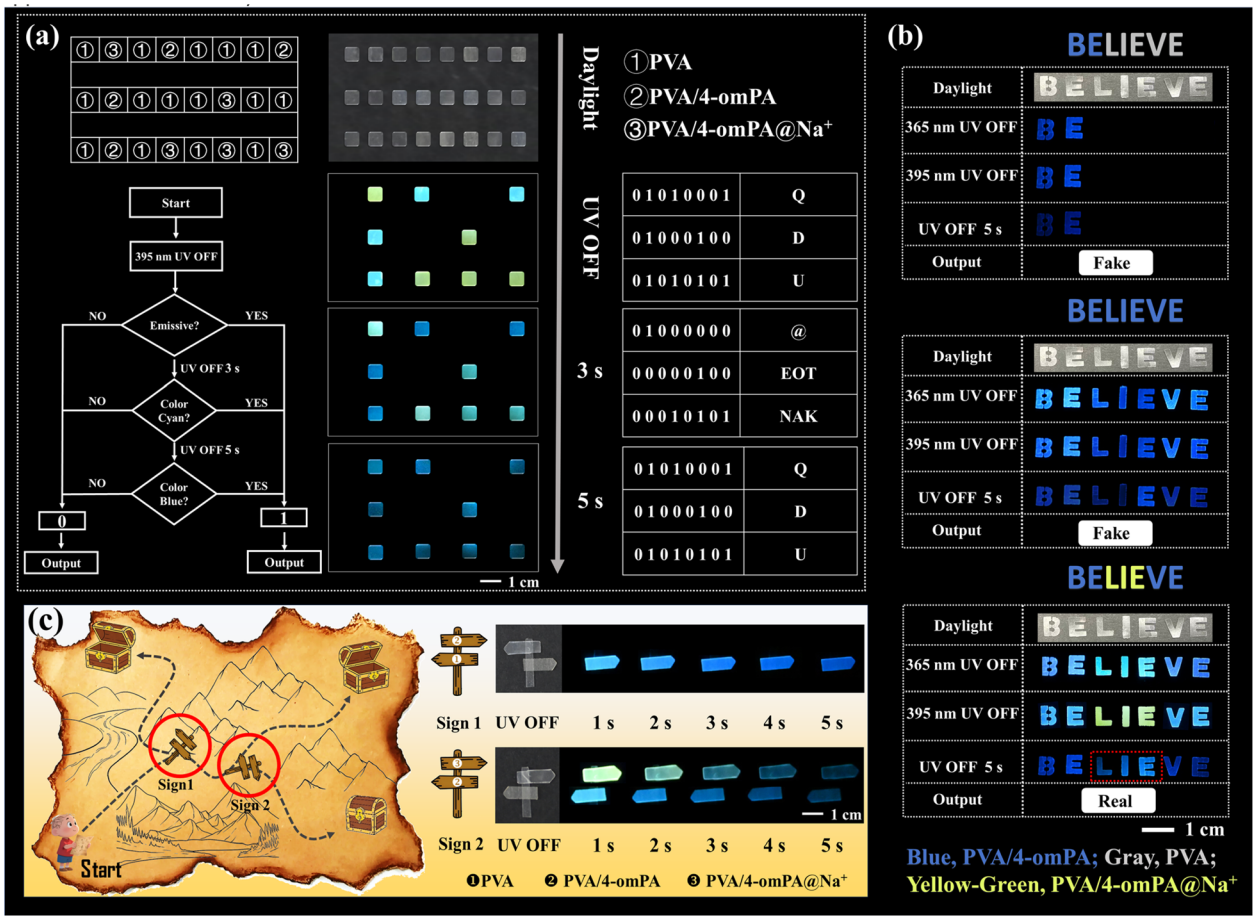

Fig. 6 Application demonstrations of the phosphorescent polymer films. (a) ASCII program encoding. (b) Anti-counterfeiting pattern based on the word "BELIEVE" fabricated from PVA, PVA/4-omPA, and PVA/4-omPA@Na^+. (c) Treasure-map guidance system constructed from the three phosphorescent materials.

phosphorescent material under the same excitation, the afterglow color transitions gradually from yellow to blue. At 3 seconds following cessation of UV illumination, the program captures the afterglow a second time and deciphers the genuinely stored and encrypted information according to the predefined condition "afterglow color is cyan". The associated ASCII codes-"01000000", "00000100", and "00010101"-translate to "@, EOT, NAK", signifying "end of transmission, reject reception". As phosphorescence persists, a third afterglow measurement is taken at 5 seconds, with the program applying the condition "afterglow color is blue", which yields the ASCII codes "01010001", "01000100", and "01010101" once more, thereby reproducing the message "QDU" and effectively re-concealing the encrypted information.

An anti-counterfeiting pattern spelling "BELIEVE" was fabricated by selectively integrating PVA, PVA/4-omPA, and PVA/4-omPA@Na^+ materials (Fig. 6b). In the first configuration, a combination of PVA and PVA/4-omPA was employed. After the UV excitation at 365 or 395 nm was switched off and allowed to decay for 5 s, the pattern only displayed the fragment "BE", corresponding to incomplete or invalid information. In the second configuration, only the PVA/4-omPA phosphorescent material was used. Under identical excitation conditions, the label consistently exhibited the complete blue word "BELIEVE", which lacks the dynamic features required for reliable information authentication. In contrast, the third configuration integrates both PVA/4-omPA and PVA/4-omPA@Na^+ phosphorescent materials. When the excitation at 365 nm is removed, the segment "LIE" in the word "BELIEVE" appears in blue. However, after excitation at 395 nm is switched off, the "LIE" region constructed from PVA/4-omPA@Na^+ initially displays yellow phosphorescence and gradually transitions to blue after a delay of 5 s. Consequently, only the pattern that exhibits the sequential cyan-yellow-blue afterglow evolution represents the authentic information, demonstrating a multilevel anti-counterfeiting strategy enabled by excitation- and time-dependent phosphorescent color switching.

Fig. 6c depicts a treasure map featuring three chests, only one of which contains treasure. At two bifurcated intersections, signposts made from two distinct types of materials are installed: signpost one consists of PVA and PVA/4-omPA materials, while signpost two is composed of PVA/4-omPA and PVA/4-omPA@Na^+ materials. Upon reaching signpost one, the treasure hunter interprets the clue "the signpost pointed to by the

© 2026 The Author(s). Published by the Royal Society of Chemistry

Open Access Article. Published on 15 April 2026. Downloaded on 5/6/2026 4:13:05 AM. This article is licensed under a Creative Commons Attribution-NonCommercial 3.0 Unported Licence.

afterglow" to determine the correct path. At the subsequent fork, the hunter follows the instruction "the signpost color has a dynamic change" to navigate toward the treasure chest and successfully retrieve the treasure. This wavelength/time-dependent dynamic multi-color afterglow property provides additional time and wavelength channels for multi-level information encryption and dynamic data storage.

Conclusions

In this work, we developed a simple and cost-effective strategy to achieve dynamic multicolor modulation in polymer-based RTP materials by introducing alkali–metal–ion regulation into a covalently crosslinked host–guest system. The PVA/4-omPA composite exhibits stable blue RTP with an ultralong lifetime of 1.38 s, which originates from the rigid environment formed by the covalent and hydrogen-bonding network between PVA and 4-omPA. Upon the introduction of NaCl, Na^+ partially perturbs the original covalent network and induces ion-bridging interactions, generating additional rigid microdomains and multiple emissive centers. Specifically, in the PVA/4-omPA@Na^+ system, the salt-induced ion-bridging network generates new emission centers at 530 and 563 nm, while the intrinsic covalent and hydrogen-bonding crosslinking between PVA and 4-omPA predominantly governs the 460 nm emission center. Owing to the distinct decay rates of these emissive centers, the composite exhibits excitation wavelength/time-dependent dynamic afterglow, evolving from cyan to blue under 365 nm excitation and from yellow-green to blue under 395 nm excitation. The resulting color-tunable RTP films combine straightforward fabrication, mechanical flexibility, and stable luminescent performance, highlighting their potential for applications in flexible displays, dynamic anti-counterfeiting, and multilevel information encryption. More importantly, this work provides new mechanistic insights and practical guidance for constructing dynamic multicolor RTP systems through ion-regulated host–guest interactions.

Author contributions

S. Yang and G. Xiao designed the project. S. Yang synthesized the samples and carried out the measurements. All authors analyzed the experimental data. S. Yang, G. Xiao and C. Xu co-wrote the manuscript.

Conflicts of interest

There are no conflicts to declare.

Data availability

The data supporting this article have been included as part of the supplementary information (SI). Supplementary information: experimental procedures, theoretical calculations, structural characteristics and measurements of optical properties. See DOI: https://doi.org/10.1039/d6sc02317g.

Acknowledgements

This work was supported by the Major Scientific and Technological Innovation Project of Shandong Province (Grant No. 2023CXGC010610), the National Natural Science Foundation of China (Grant No. 22405148) and the Shandong Provincial Natural Science Foundation (Grant No. ZR2024QB084).

Notes and references

1 X. Yao, Y. Li, H. Shi, Z. Yu, B. Wu, Z. Zhou, C. Zhou, X. Zheng, M. Tang, X. Wang, H. Ma, Z. Meng, W. Huang and Z. An, *Nat. Commun.*, 2024, **15**, 4520.
2 S. Hu, W. Zhang, K. Wang, H. Ma, X. Wang, Z. An and W. Huang, *Angew. Chem., Int. Ed.*, 2026, **65**, e23080.
3 G. Xiao, X. Fang, Y.-J. Ma and D. Yan, *Adv. Sci.*, 2022, **9**, 2200992.
4 X. Wang, Z. Zhang, S. Yang, J. Du, Y. Jiang, D. Miao, S. Chen, Z. Xiang, G. Xiao, C. Xu and S. Ramakrishna, *ACS Mater. Lett.*, 2025, **7**, 928–937.
5 G. Xiao, X. Wang, X. Fang, J. Du, Y. Jiang, D. Miao, D. Yan and C. Xu, *Chem. Sci.*, 2024, **15**, 17224–17231.
6 B. Ding, L. Ma, Z. Huang, X. Ma and H. Tian, *Sci. Adv.*, 2021, **7**, eabf9668.
7 Y. Liang, Y. Shang, K. Liu, Z. Liu, W. Wu, Q. Liu, Z. Qi, X. Wu, L. Dong and C. Shan, *Nano Res.*, 2020, **13**, 875–881.
8 H. Deng, G. Li, H. Xie, Z. Yang, Z. Mao, J. Zhao, Z. Yang, Y. Zhang and Z. Chi, *Angew. Chem., Int. Ed.*, 2024, **63**, e202317631.
9 M. Zhu, X. Xu, Q. Wang, S. Han, Y. Ma and J. Li, *Coord. Chem. Rev.*, 2026, **550**, 217418.
10 S. Feng, Q. Huang, S. Yang, Z. Lin and Q. Ling, *Chem. Sci.*, 2021, **12**, 14451.
11 J. Chen, T. Yu, E. Ubba, Z. Xie, Z. Yang, Y. Zhang, S. Liu, J. Xu, M. P. Aldred and Z. Chi, *Angew. Chem., Int. Ed.*, 2020, **59**, 10032.
12 R. Chen, Y. Guan, H. Wang, Y. Zhu, X. Tan, P. Wang, X. Wang, X. Fan and H. Xie, *ACS Appl. Mater. Interfaces*, 2021, **13**, 41131–41139.
13 J. Ma, S. Li, W. Yang, Y. Chang, Y. Zhao, H. Li, R. He, D.-B. Kuang and L. Zhou, *Angew. Chem., Int. Ed.*, 2026, **65**, e24854.
14 Y. Peng, J. Ma, Y. Zhao, D. You, Y. Yao, Z. Deng, J. Liao, Y. Chang, W. Shen, M. Li, R. He and L. Zhou, *Adv. Funct. Mater.*, 2025, **35**, 2420311.
15 S. Zong, J. Zhang, X. Yin, J. Li and S. Qu, *Nano Lett.*, 2024, **24**, 1859–1866.
16 M. Shi, Q. Gao, M. Chen, Z. Lv, J. Rao, G. Chen, B. Lue, W. Qi, J. Ren and F. Peng, *Nat. Commun.*, 2025, **16**, 7473.
17 L. Zhang, X. Chen, M. Xin, H. Yang, D. Guo and Y. Hu, *Small*, 2024, **20**, 2406596.
18 L. Zhou, K. Li, Y. Chang, Y. Yao, Y. Peng, M. Li and R. He, *Chem. Sci.*, 2024, **15**, 10046–10055.
19 W. Yu, C. Li, X. Zhao, M. Zhang, W. Ye, Y. Shi, B. Wu, H. Sun and L. Zhu, *Angew. Chem., Int. Ed.*, 2026, **65**, e1607487.
20 J.-H. Chen, J.-B. Luo, Q.-P. Peng, Z.-L. He, J.-H. Wei and D.-B. Kuang, *Angew. Chem., Int. Ed.*, 2025, **64**, e202508536.

Open Access Article. Published on 15 April 2026. Downloaded on 5/6/2026 4:13:05 AM. This article is licensed under a Creative Commons Attribution-NonCommercial 3.0 Unported Licence.

21 H. Xie, J. Wang, Z. Lou, L. Hu, S. Segawa, X. Kang, W. Wu, Z. Luo, R. T. K. Kwok, J. W. Y. Lam, J. Zhang and B. Z. Tang, *J. Am. Chem. Soc.*, 2024, **146**, 18350–18359.
22 Z. Xiong, X. Liu, Z. Zhang, S. Wei, J. Liu, Q. Xu, J. Z. Sun, J. Zhang, B. Z. Tang and H. Zhang, *Chem*, 2026, **12**, 102858.
23 Y. Xia, C. Zhu, F. Cao, Y. Shen, M. Ouyang and Y. Zhang, *Angew. Chem., Int. Ed.*, 2023, **62**, e202217547.
24 L. Gu, H. Wu, H. Ma, W. Ye, W. Jia, H. Wang, H. Chen, N. Zhang, D. Wang, C. Qian, Z. An, W. Huang and Y. Zhao, *Nat. Commun.*, 2020, **11**, 944.
25 Q. Wang, X. Xu, M. Zhu, Y. Du, Y. Ma, J. Li and G. Wang, *Chem. Eng. J.*, 2025, **507**, 160535.
26 Z. Wang, L. Zhang, M. Dong, Y. Xie, P. Yu, X. Guo, F. Liang, J. Zhao and Y. Geng, *J. Mater. Chem. C*, 2024, **12**, 17135–17143.
27 C. Zhang, L. Lou, Y. Li, S. Sun, W. Hu, K. Wang, D. Wang, H. Cao, W. He and Z. Yang, *J. Phys. Chem. C*, 2023, **127**, 20929–20938.
28 F. Xiao, H. Gao, Y. Lei, W. Dai, M. Liu, X. Zheng, Z. Cai, X. Huang, H. Wu and D. Ding, *Nat. Commun.*, 2022, **13**, 186.
29 Y. Zhang, Y. Su, H. Wu, Z. Wang, C. Wang, Y. Zheng, X. Zheng, L. Gao, Q. Zhou, Y. Yang, X. Chen, C. Yang and Y. Zhao, *J. Am. Chem. Soc.*, 2021, **143**, 13675–13685.
30 D. Li, Y. Yang, J. Yang, M. Fang, B. Tang and Z. Li, *Nat. Commun.*, 2022, **13**, 147.
31 Z. Liang, M. Wei, S. Zhang, W. Huang, N. Shi, A. Lv, H. Ma and Z. He, *ACS Appl. Mater. Interfaces*, 2023, **15**, 35534–35542.
32 L. Zhou, K. Li, Y. Chang, Y. Yao, Y. Peng, M. Li and R. He, *Chem. Sci.*, 2024, **15**, 10046–10055.
33 W. Dai, Y. Jiang, Y. Lei, X. Huang, P. Sun, J. Shi, B. Tong, D. Yan, Z. Cai and Y. Dong, *Chem. Sci.*, 2024, **15**, 4222–4237.
34 P. Wix, S. Tandon, S. Vaesen, K. Karimu, J. Mathieson, K. Esien, S. Felton, G. Watson and W. Schmitt, *Nat. Commun.*, 2024, **15**, 10180.
35 R. Tian, S. Gao, K. Li and C. Lu, *Nat. Commun.*, 2023, **14**, 4720.
36 R. Wang, D. Ma, X. Kong, F. Peng, X. Cao, Y. Zhao, C. Lu and W. Shi, *Angew. Chem., Int. Ed.*, 2024, **136**, e202409162.
37 W. Qiao, K. Chang, X. Yu, Z. Zhao, N. Zhao, B. Li, Q. Li, Z. Li and Z. Li, *Angew. Chem., Int. Ed.*, 2026, **65**, e23121.
38 Y. Wang, J. Yang, M. Fang, Y. Yu, B. Zou, L. Wang, Y. Tian, J. Cheng, B. Z. Tang and Z. Li, *Matter*, 2020, **3**, 449–463.
39 Y. Zhang, M. Gao, R. Wu, Y. Meng, N. Li, Z. Chen, M. Fang, J. Yang and Z. Li, *Adv. Funct. Mater.*, 2025, **35**, 2502811.
40 C. Chen, Y. Yang, L. Zhang, W. Dai, Y. Lei, M. Liu, H. Wu, X. Huang and D. Yan, *Nat. Commun.*, 2026, **17**, 1870.
41 Z. Qi, M. Dai, Y.-J. Ma and D. Yan, *Angew. Chem., Int. Ed.*, 2025, **64**, e2025.
42 Z. Y. Wang, Z. Yin, Q. Hu, D. Yan and J. Xiao, *Angew. Chem., Int. Ed.*, 2026, **65**, e23858.
43 R. Gao, Q. Zhao, B. Zeng, X. Liu, Y. Xu, C. Yuan and L. Dai, *ACS Appl. Nano Mater.*, 2025, **8**, 9387–9399.
44 S. Choe, S. You, K. Park, Y. Kim, J. Park, Y. Cho, J. Seo, H. Yang and J. Myung, *Green Chem.*, 2024, **26**, 8230–8241.
45 O. Tretinnikov and S. Zagorskaya, *Polym. Sci., Ser. A*, 2013, **55**, 463–470.
46 Y. Oyarzún, J. Ulloa, M. Ceballos and B. F. Urbano, *Gels*, 2024, **10**, 504.
47 L. Lambertini, G. Coccarelli, E. Toto, M. Santonicola and S. Laurenzi, *Acta Astronaut.*, 2024, **221**, 142–154.
48 A. Pal, R. Chauhan, B. Roy, S. Maiti, S. Chowdhury, J. Nayak, M. Pullela, S. Ray, S. Chattopadhyay and N. Das, Design of ZIF-8-Reinforced Dynamically Cross-Linked Hydrogel Electrolyte for Robust and Flexible Supercapacitor Devices, *ACS Appl. Polym. Mater.*, 2025, **7**, 15176–15193.
49 L. Xin, Y. Cai, J. Liu, W. Jia, L. Fang and C. Liu, *Int. J. Biol. Macromol.*, 2024, **281**, 136433.

© 2026 The Author(s). Published by the Royal Society of Chemistry